RAA 2016 Vol. **16** No. **10**, 158 (10pp) doi: 10.1088/1674–4527/16/10/158
http://www.raa-journal.org *http://iopscience.iop.org/raa*

Research in Astronomy and Astrophysics

Sky reconstruction for the Tianlai cylinder array

Jiao Zhang[1,2,3], Shi-Fan Zuo[1,3], Reza Ansari[2], Xuelei Chen[1,3,4] ,Yi-Chao Li[1,3], Feng-Quan Wu[1,3], Jean-Eric Campagne[2] and Christophe Magneville[5]

[1] Key Laboratory of Computational Astrophysics, National Astronomical Observatories, Chinese Academy of Sciences, Beijing 100012, China; *xuelei@cosmology.bao.ac.cn*
[2] Université Paris-Sud, LAL, UMR 8607, F-91898 Orsay Cedex, France & CNRS/IN2P3, F-91405 Orsay, France
[3] University of Chinese Academy of Sciences, Beijing 100049, China
[4] Center for High Energy Physics, Peking University, Beijing 100871, China
[5] CEA, DSM/IRFU, Centre d'Etudes de Saclay, F-91191 Gif-sur-Yvette, France

Received 2016 May 5; accepted 2016 June 3

Abstract We apply our sky map reconstruction method for transit type interferometers to the Tianlai cylinder array. The method is based on spherical harmonic decomposition, and can be applied to a cylindrical array as well as dish arrays and we can compute the instrument response, synthesized beam, transfer function and noise power spectrum. We consider cylinder arrays with feed spacing larger than half a wavelength and, as expected, we find that the arrays with regular spacing have grating lobes which produce spurious images in the reconstructed maps. We show that this problem can be overcome using arrays with a different feed spacing on each cylinder. We present the reconstructed maps, and study the performance in terms of noise power spectrum, transfer function and beams for both regular and irregular feed spacing configurations.

Key words: cosmology: observation — HI intensity mapping — method: transit telescope — map making

1 INTRODUCTION

Determination of the neutral hydrogen (HI) distribution from 21 cm line observation is an important method to study the statistical properties of large scale structures in the Universe. The intensity mapping technique is an efficient and economical way to map the Universe using (HI) 21 cm emission, which is suitable for late time cosmological studies ($z \lesssim 3$), especially for constraining dark energy models through baryon acoustic oscillation (BAO) features (Peterson et al. 2006; Chang et al. 2008; Ansari et al. 2008, 2012; Seo et al. 2010; Gong et al. 2011). Large wide field and wide band radio telescopes would be needed to rapidly acquire observations of large volumes of the Universe. Several dedicated experiments are aimed at such surveys, including our own experiment Tianlai[1] (Chen 2012), as well as CHIME (Bandura et al. 2014), BINGO (Battye et al. 2013), HIRAX[2] and BAORadio[3].

In transit mode intensity mapping surveys, the antennas are fixed on the ground during operation, observing the sky as the Earth rotates. For cylinder arrays such as Tianlai and CHIME, the instantaneous field of view is a strip of sky along the meridian, and sky patches with different right ascensions pass through the field of view. As the telescopes do not need to track a particular celestial target, the mechanical structure of the telescope is very simple.

The Tianlai project is designed to survey large scale structures by intensity mapping of the redshifted 21 cm line, and to constrain dark energy models by BAO measurement. As a first step, the current pathfinder experiment will test the basic principles and key technologies of the 21 cm intensity mapping method. The Tianlai array is a wide band interferometer which features both a cylinder array and a dish array, installed at a radio quiet site ($44^\circ 10' 47''$N, $91^\circ 43' 36''$E) in Hongliuxia, Balikun County, Xinjiang Uygur Autonomous Region in Northwest China (Chen 2015). The construction of the Tianlai cylinder and dish pathfinder arrays were completed at the end of 2015, and the two arrays are now undergoing their commissioning process. The map making algorithm and its application to dish arrays have been presented in Zhang et al. (2016), hereafter referred to as Paper I. In the present paper, we will focus on its application to the Tianlai pathfinder cylinder array.

The Tianlai cylinder pathfinder array has three adjacent cylindrical reflectors oriented in the North-South (NS) direction. Each cylinder is 15 m wide and 40 m long. At present, the cylinders are equipped with a total of 96 dual

[1] *http://tianlai.bao.ac.cn*
[2] *http://www.acru.ukzn.ac.za/cosmosafari/wp-content/uploads/2014/08/Sievers.pdf*
[3] *http://groups.lal.in2p3.fr/bao21cm*

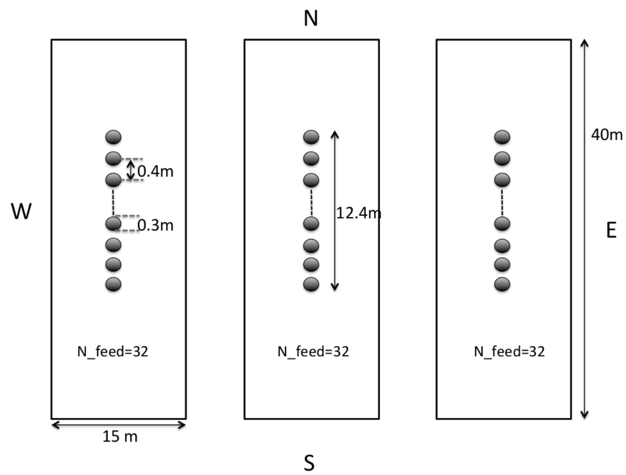

Fig. 1 Regular configuration of the cylinder array.

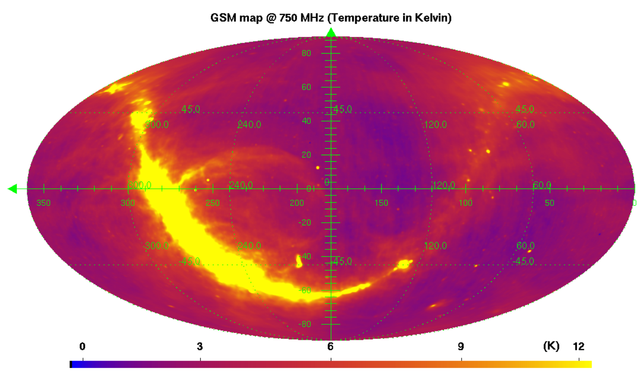

Fig. 2 GSM map at 750 MHz, used as the true sky for reconstruction with the Tianlai cylinder configuration.

polarization receivers which do not cover the full length of the cylinders. In the future, the pathfinder instrument may be upgraded by simply adding more feed units and associated electronics. The longer term plan is to expand the Tianlai array to full scale once the principle of intensity mapping is proven to work. The full scale Tianlai cylinder array would have a collecting area of $\sim (10^4\,\mathrm{m})^2$ and $\sim 10^3$ receiver units. A forecast for its capability in measuring dark energy and constraining primordial non-Gaussianity can be found in Xu et al. (2015). In addition to the redshifted 21 cm intensity mapping observation, such surveys may also be used for other observations, such as 21 cm absorbers (Yu et al. 2014), fast radio bursts (Masui et al. 2015; Connor et al. 2016), and electromagnetic counterparts of gravitational wave events (Feng et al. 2014).

The simplest arrangement of the existing 96 feeds is to have 32 feeds on each cylinder, regularly spaced so that on each cylinder the feeds form a uniformly spaced linear array. Two such configurations are considered here:

(1) **Regular 1.** The feed spacing is taken to be $d_{\rm sep} = 0.4\,\mathrm{m}$, which is about one wavelength at the observation frequency of 750 MHz. In this configuration, the feeds occupy only $12.4\,\mathrm{m}$ of the total $40\,\mathrm{m}$ length of the cylinder, as shown in Figure 1.

(2) **Regular 2.** The feed spacing is taken to be $d_{\rm sep} = 0.8\,\mathrm{m}$, about twice the wavelength at the cylinder.

One may also consider configurations with irregular positioning of the feeds to reduce grating lobes. In this paper we consider a very simple extension: on each cylinder the feeds still form a uniform linear array, but the number of feeds and hence the spacing of the array is different on each cylinder. We have a total of 96 feeds at the present time. Marking the cylinders from East to West as Cylinder 1, Cylinder 2 and Cylinder 3 respectively, we consider the following configurations:

(1) **Irregular 1.** This is the first irregular cylinder array with number of feeds on each cylinder being 31, 32 and 33 respectively. The feeds occupy $12.4\,\mathrm{m}$ along the NS direction on each cylinder. The feed spacing would be $d_{\rm sep} = 0.413\,\mathrm{m}$ for Cylinder 1, $d_{\rm sep} = 0.4\,\mathrm{m}$ for Cylinder 2 and $d_{\rm sep} = 0.388\,\mathrm{m}$ for Cylinder 3.

(2) **Irregular 2.** This is the second irregular cylinder array with number of feeds on each cylinder being 31, 32 and 33 respectively, but the feeds occupy 24.8 m along the NS direction on each cylinder. The feed spacing would be $d_{\rm sep} = 0.827\,\mathrm{m}$ for Cylinder 1, $d_{\rm sep} = 0.8\,\mathrm{m}$ for Cylinder 2 and $d_{\rm sep} = 0.775\,\mathrm{m}$ for Cylinder 3.

To simulate the map making process, we use an input map based on the Global Sky Model (GSM) (de Oliveira-Costa et al. 2008), shown in Figure 2. The map is obviously dominated by radiation from the Galactic plane, which is mostly synchrotron emission from Galactic cosmic ray electrons. For the computations carried out in this work, we have used HEALPix (Górski et al. 2005) to pixellate the celestial sphere, with $n_{\rm side} = 512$. In our spherical harmonics transformation we take $\ell_{\max} = 1500$, which is sufficient for the angular resolution of the Tianlai pathfinder cylinder array.

Section 2 provides a brief review of the spherical harmonic decomposition map making method. In Section 3 we discuss the grating lobe problems and spurious image regular receivers layout. To resolve these problems, in Section 4 we study the case of irregular layouts listed above. We present our conclusion in Section 5.

2 A BRIEF REVIEW OF THE SKY RECONSTRUCTION METHOD

In this section, we briefly present the map making method for a transit interferometer array based on spherical harmonic decomposition. A more detailed presentation and comparison with classical radio interferometry (tracking type surveys) can be found in Paper I, as well as in Shaw et al. (2014). Unlike frequently used tracking observations, it is more convenient to work in ground coordinates in which the baselines of the array do not change during the transit observation. In this formalism, the visibilities recorded as a function of time correspond to observations of different parts of the sky. We separate the inversion problem into independent sub-systems using m-mode decomposition in spherical harmonics and we assume that the individual feed responses and array geometry are known. The sky emission intensity is $I(\hat{\boldsymbol{n}}) = \langle \boldsymbol{E}^*(\hat{\boldsymbol{n}}, t)\cdot\boldsymbol{E}(\hat{\boldsymbol{n}}, t)\rangle_t$, where $\hat{\boldsymbol{n}} = (\alpha, \delta)$ denotes the sky direction, and the receivers are sensitive to the complex amplitudes of sky emission $\boldsymbol{E}(\hat{\boldsymbol{n}})$. A single receiving element can be characterized by its complex angular response $D(\hat{\boldsymbol{n}})$ and its position $\boldsymbol{r}$, so the output of element j is

$$s_j(t) = \iint d\hat{\boldsymbol{n}}\, D_j(\hat{\boldsymbol{n}}, t)\, E(\hat{\boldsymbol{n}}, t)\, e^{i\boldsymbol{k}\cdot\boldsymbol{r_j}}\,. \tag{1}$$

The visibility $V_{ij} = \langle s_i^*\ s_j\rangle_t$ is the short term average of the cross correlation of the outputs of a pair of antennae or feeds s_i, s_j, located at positions $\boldsymbol{r_i}, \boldsymbol{r_j}$ with $\boldsymbol{r_{ij}} \equiv \boldsymbol{r_j} - \boldsymbol{r_i}$. Since emissions from different directions of the sky are incoherent, only the waves from the same direction are correlated, and the integration yields the interferometer equation

$$V_{ij} \;=\; \iint D_i^*(\hat{\boldsymbol{n}})\, D_j(\hat{\boldsymbol{n}})\, I(\hat{\boldsymbol{n}})\, e^{i\boldsymbol{k}\cdot\boldsymbol{b_{ij}}}\, d\hat{\boldsymbol{n}} \tag{2}$$

$$\;=\; \iint L_{ij}(\hat{\boldsymbol{n}})\, I(\hat{\boldsymbol{n}})\, d\hat{\boldsymbol{n}}. \tag{3}$$

In a transit instrument, visibilities are measured as a function of time or right ascension, with the beam response $L_{ij}(\hat{\boldsymbol{n}})$ changing due to Earth's rotation. In discrete form, including the contribution of noise and gathering visibility measurements from all baselines and from all times into a vector, we can write the full measurement equation in matrix form

$$[\mathrm{V}] = [\mathbf{L}][\mathrm{I}] + [n], \tag{4}$$

where we have used square brackets to emphasize these are vectors and matrices, and the time ordered visibility data [V] are linearly related to the sky intensity from different directions [I] by the time dependent beam response represented as matrix [$\mathbf{L}$]. The map making process for the interferometer array solves this system and reconstructs [I] from the observed time ordered visibility data.

We expand the sky intensity and beam response into spherical harmonics,

$$I(\hat{\boldsymbol{n}}) \;=\; \sum_{\ell=0}^{+\infty}\sum_{m=-\ell}^{+\ell} \mathcal{I}_{\ell,m}\, Y_{\ell,m}(\hat{\boldsymbol{n}}), \tag{5}$$

$$L_{ij}(\hat{\boldsymbol{n}}) \;=\; \sum_{\ell=0}^{+\infty}\sum_{m=-\ell}^{+\ell} \mathcal{L}_{\ell,m}\, Y_{\ell,m}(\hat{\boldsymbol{n}}). \tag{6}$$

where (θ, ϕ) are polar coordinates, $\theta = 90^\circ - \delta$ and $\phi = \alpha$. $Y_{\ell,m}(\hat{\boldsymbol{n}})$ are spherical harmonic functions. Then the visibilities can also be written as a summation of spherical harmonic modes,

$$V_{ij} = \sum_{\ell,m} (-1)^m \mathcal{I}_{\ell,m}\, \mathcal{L}_{\ell,-m}\,.$$

For the transit interferometer array, the effect of Earth's rotation is that the beam $L_{ij}(\hat{\boldsymbol{n}})$ has a constant drift along the right ascension direction, with the offset angle given by $\alpha_p(t) = \alpha_0 + \Omega_e\, t$, where Ω_e is angular rotation rate of the Earth, so that

$$L_{ij}(\hat{\boldsymbol{n}}, t) = L_{ij}((\theta, \varphi), t) = L_{ij}(\theta, \varphi - \alpha_p(t)). \tag{7}$$

The spherical harmonic coefficients of the rotated/shifted beams can be written as $\mathcal{L}_{\ell,m}(t_k) = \mathcal{L}_{\ell,m} e^{-im\alpha_p(t)}$. The recorded visibilities as a function of α_p are then

$$V_{ij}(\alpha_p) \;=\; \sum_{m=-\infty}^{+\infty}\sum_{\ell=|m|}^{+\infty} (-1)^m\, \mathcal{I}_{\ell,m}\, \mathcal{L}_{\ell,-m}\, e^{im\alpha_p}\,. \tag{8}$$

We recognize this expression as a Fourier series for the periodic function $V_{ij}(\alpha_p)$; the corresponding Fourier coefficients $\tilde{\mathcal{V}}_{ij}(m)$, computed from a set of regularly time sampled visibility measurements, are

$$\tilde{V}_{ij}(m) = (-1)^m \sum_{\ell=|m|}^{+\ell_{\max}} \mathcal{I}_{\ell,m}\, \mathcal{L}_{\ell,-m} + \text{noise}\,. \tag{9}$$

Grouping m-mode visibilities from all baselines in a vector and using matrix notation, we can write the measurement equation for each m-mode as

$$\left[\tilde{V}_{ij}\right]_m \;=\; \mathbf{L}_{ij,m} \;\times\; [\mathcal{I}(\ell)]_m + [\tilde{n}_{ij}]_m\;, \tag{10}$$

or putting all baselines of the array together,

$$\left[\tilde{V}\right]_m \;=\; \mathbf{L}_m \;\times\; [\mathcal{I}(\ell)]_m + [\tilde{\mathbf{n}}]_m\;. \tag{11}$$

By comparing with Equation (4), the full linear system is decomposed into a set of $m_{\max} = \ell_{\max}$ independent smaller systems, one for each m-mode, which have much smaller dimensions ($n_{\text{baseline}} \times \ell_{\max}$) and are thus much easier to solve numerically.

We assume that the noise associated with the visibility measurement follows a Gaussian random process, with variance $\mathbf{N} = \langle nn^\dagger\rangle$. Using the maximum likelihood method, the solution of the observed sky is given by

$$[\widehat{\mathcal{I}}]_m = \mathbf{L}_m^{-1}\,[\tilde{V}]_m\,, \tag{12}$$

where $\mathbf{L}_m^{-1}$ denotes the noise weighted pseudo-inverse matrix of $\mathbf{L}_m$. This can be computed by using the singular value decomposition (SVD) method, in which any $m \times n$ matrix $\mathbf{A}$ can be decomposed as $\mathbf{A} = \mathbf{U\Sigma Q}^\dagger$, where $\mathbf{U}$ and $\mathbf{Q}$ are $m \times m$ and $n \times n$ unitary matrices respectively, and $\mathbf{\Sigma}$ is an $m \times n$ rectangular diagonal matrix; i.e., all non-diagonal elements are zero, with non-negative real numbers on the diagonal. The pseudo-inverse is given by

$$\tilde{\mathbf{A}}^{-1} = \mathbf{Q}\tilde{\mathbf{\Sigma}}^{-1}\mathbf{U}^\dagger\,, \tag{13}$$

where $\tilde{\mathbf{\Sigma}}^{-1}$ is obtained by replacing all diagonal elements e_{ii} above a certain threshold value by their reciprocal $1/e_{ii}$, while setting the other elements to zero. For details on computing the pseudo-inverse, see e.g. Barata & Hussein (2012).

By substituting Equation (11) into Equation (12), and neglecting noise, we have $\hat{\mathcal{I}} = \mathcal{R}\mathcal{I}$, where $\mathcal{R}$ denotes the reconstruction or response matrix, which relates the reconstructed sky to the original sky. In the spherical harmonic representation, the m-mode reconstruction matrix is $\mathbf{R}_m \equiv \tilde{\mathbf{L}}_m^{-1}\mathbf{L}_m$. Ideally, if $\mathbf{R}_m = \mathbf{I}$ then the reconstruction for the m-mode is completely accurate. In practice, the reconstruction is usually not fully accurate.

For each given m, the different ℓ coefficients are correlated and the physical measurement data are a mix of different ℓ mode contributions. We can define the compressed response matrix $\mathbf{R}$ by extracting the diagonal terms from individual $\mathbf{R}_m$ matrices

$$\mathbf{R}(\ell, m) \;=\; \mathbf{R}_m(\ell, \ell)\,.$$

Obviously, $\mathbf{R}(\ell, m)$ does not fully describe the reconstruction in the (ℓ, m) plane and the original $\mathbf{R}_m$ matrices are needed. However, the $\mathbf{R}(\ell, m)$ matrix can give some idea of how well an (ℓ, m) mode is measured with a given array configuration, so it can help us to compare the performance of different configurations.

If we consider the reconstruction of sky spherical harmonic coefficients from pure noise visibilities ($\tilde{\mathrm{V}}_{ij} = \tilde{n}_{ij}$), the covariance matrix $\mathbf{Cov}(\ell_1, \ell_2)$ of the estimator $\widehat{\mathcal{I}}(\ell, m)$ for each mode m can be computed from the $\mathbf{L}_m^{-1}$ matrix and the noise covariance matrix $\mathbf{N}_m = [\tilde{\mathrm{n}}_{ij}]_m \cdot [\tilde{\mathrm{n}}_{ij}]_m^\dagger$,

$$\begin{aligned}\mathbf{Cov}_m(\ell_1, \ell_2) \;&=\; \left\langle \left[\widehat{\mathcal{I}}(\ell)\right]_m \cdot \left[\widehat{\mathcal{I}}(\ell)\right]_m^\dagger \right\rangle \\ &=\; \mathbf{L}_m^{-1}\,\mathbf{N}_m\,\mathbf{L}_m^{-1\dagger}\,.\end{aligned}$$

The covariance matrix is not diagonal, especially due to partial sky coverage in declination. However, if we ignore this correlation and only use the diagonal terms for each m mode, we can gather them together to create the $\sigma_{\mathcal{I}}^2(\ell, m)$ variance matrix. This matrix informs us on how well each (ℓ, m) mode is measured.

$$\sigma_{\mathcal{I}}^2(\ell, m) \;=\; \mathbf{Cov}_m(\ell, \ell)\,. \tag{14}$$

We consider a survey duration of two full years for the results presented in this paper. The total integration time for each visibility time sample would be $t_{\rm int} \sim 2 \times 10^4\,$s for $n_t = 2m_{\rm max} = 3000$. Assuming a system temperature $T_{\rm sys} = 50\,$K and $\Delta\nu = 1$ MHz, the effective $\sigma_{\rm noise}$ for measured visibility time samples can then be written as a function of integration time per time sample $t_{\rm int}$,

$$\sigma_{\rm noise} \;=\; \frac{\sqrt{2}T_{\rm sys}}{\sqrt{t_{\rm int}\,\Delta\nu}} \sim 0.49\,\mathrm{mK}\,. \tag{15}$$

3 THE REGULAR ARRAY CONFIGURATION

The primary beam for each feed on the cylinders is narrow in the East-West (EW) direction and wide in the NS direction, as determined by the curvatures of the cylindrical reflector. We model the primary beam of a single feed associated with a cylindrical reflector as

$$D(\alpha, \beta) \propto \frac{\sin(\alpha\pi(L_x/\lambda))}{\alpha\pi(L_x/\lambda)}\frac{\sin(\beta\pi(L_y/\lambda))}{\beta\pi(L_y/\lambda)}\,, \tag{16}$$

where (α, β) are the two angles with respect to the feed axis, along the EW and NS planes respectively. λ is the wavelength, and L_x and L_y are the effective feed sizes along the EW and NS planes respectively. We take $L_y = 0.3\,$m for the Tianlai cylinder feeds, and $L_x = 13.5\,$m corresponds to an illumination efficiency of 0.9 for the feed on a 15 m wide cylinder. These parameters give a beam width of $\sim 100^\circ$ in the NS direction and $\sim 2^\circ$ in the EW direction at 750 MHz. The actual values will be obtained by fitting the real observational data. These are heuristic values but should be sufficient for our estimations here. The primary beam is shown in the left panel of Figure 3.

For uniformly spaced linear arrays, grating lobes appear when the spacing is larger than half a wavelength ($d_{\rm sep} > \lambda/2$). This is because the phase factor $\exp(i2\pi d_{\rm sep}\sin\theta/\lambda)$ is periodic with respect to $\sin\theta$, and when $d_{\rm sep} > \lambda/2$ the maximum appears more than once. We show the synthesized beam for the Regular 1 case and Regular 2 case in the central and right panels respectively in Figure 3. These are obtained by constructing the full synthesis of a point source image located at the latitude of the array, i.e., $44^\circ 10'$. As we can see in the figure, there are strong grating lobes along the NS direction in the synthesized beams. The position of the nth order grating lobe is $\sim n\lambda/d_{\rm sep}$. At 750 MHz, the positions are $\pm 57.3°$ for the Regular 1 case ($d_{\rm sep} = 0.4\,$m) and $\pm 28.6°$ for the Regular 2 case ($d_{\rm sep} = 0.8\,$m). In addition, there are also primary beam side lobes along both the NS and EW directions. These are less prominent and have smaller periods.

To have a better understanding of the synthsized beams in spherical harmonic space, let us consider the beams of a single pair of receivers.

In Figure 4 we show the beam patterns for four cases: the autocorrelation (top left), and the cross-correlations for a due EW baseline between two cylinders (top right), for a due NS baseline (bottom left), and a Southeast-Northwest (SE-NW) baseline (bottom right). By definition, only the region $-\ell < m < \ell$ has valid values. In the dish case (see Paper I), the autocorrelation covers a triangular region with the top at the origin $(\ell, m) = (0, 0)$, two sides and extending along $m = \pm\ell\cos\delta$ where δ is declination of the observation, and up to $\ell_{\rm max} = 2\pi D/\lambda$ where D is the effective aperture. The autocorrelation in the cylinder case is very different, assuming a butterfly shape. This is because a cylinder's primary beam is asymmetric in the NS and EW directions. As described in Equation (16), along the NS direction which corresponds to $m \sim 0$, the primary beam has very low resolution, but along the EW direction the cylinder primary beam is about $\sim 2^\circ$ at 750 MHz, which corresponds to $\ell \sim 2\pi L_x/\lambda \sim 210$. Indeed, the figure shows that the autocorrelation function extends substantially to $\ell \sim 210$ along the two wings. Also, since the cylinder has almost the whole observable sky in its field of view, which includes the equator, the case $m = \pm\ell$ is saturated.

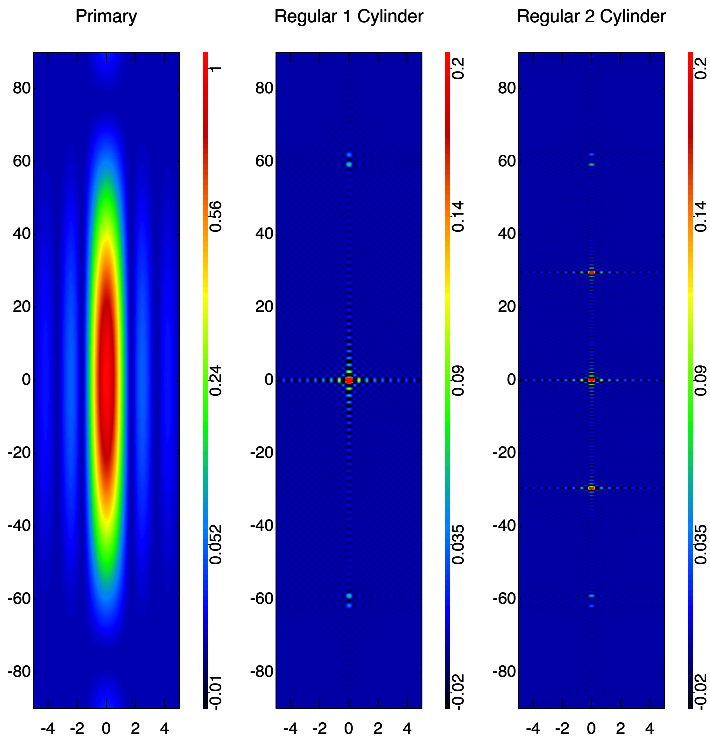

Fig. 3 The primary beam (*left*) and synthesized beams for the Regular 1 (*center*) and Regular 2 (*right*) configurations.

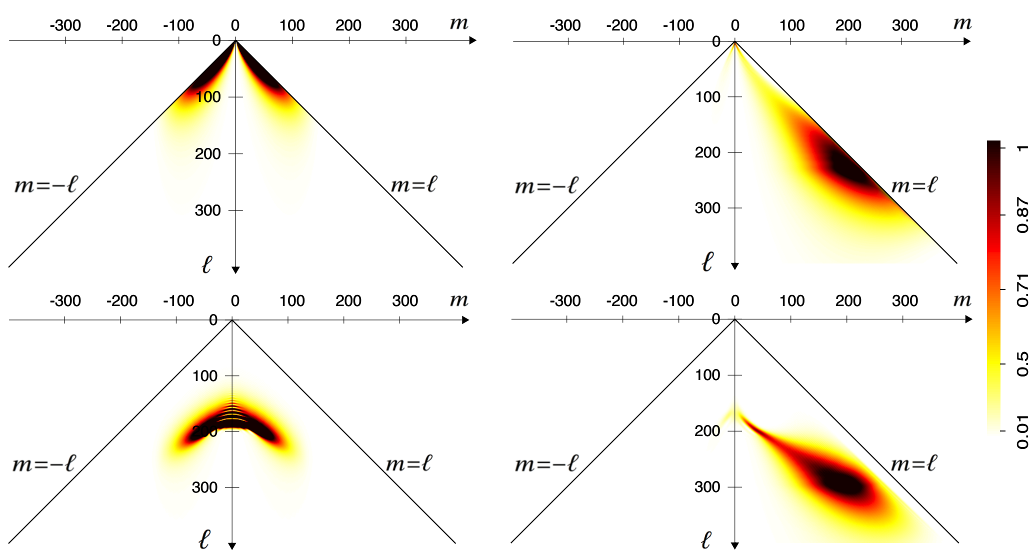

Fig. 4 The beam patterns in terms of spherical harmonics $\mathcal{L}_{\ell,m}$ with size $L_x = 13.5$ m, $L_y = 0.3$ m and centered at latitude 44.15°. Top left: autocorrelation of a feed; Top right: cross-correlation for an EW baseline with $d_{\rm sep} = 15$ m; Bottom left: cross-correlation beam for an NS baseline with $d_{\rm sep} = 12$ m; Bottom right: cross-correlation for a SE-NW baseline with $(\Delta x, \Delta y)$ =(15 m, 12 m).

For the cross-correlations, the beam pattern centers are at $(\ell, m) \sim (2\pi|\boldsymbol{u}|, 2\pi u)$ as expected, where $\boldsymbol{u} \equiv (u, v, w) = (b_x, b_y, b_z)/\lambda$. So, the EW baseline is centered near $m \sim \ell$, while the NS one is centered near $m = 0$, with $\ell \sim 2\pi b/\lambda$. Note that here we are only plotting the positive part of the baseline in one direction, so for the EW baseline the beam is on the $m > 0$ side. If we would like to plot the reverse direction, it would appear on the symmetric position at $m < 0$.

Figure 5 shows the response matrix $\mathbf{R}(\ell, m)$ for the two regular configurations at frequency 750 MHz. In Paper I, we noted that for each baseline the $\mathbf{R}$ matrix has a certain distribution centered at $(\ell, m) = 2\pi b/\lambda$, where b is the baseline length. The m position depends on both the EW component of the baseline and the declination of the strip to be observed. For an array with many baselines, the $\mathbf{R}$ matrix is described well by the superposition of these individual baselines. For the cylinder array, the field of view is

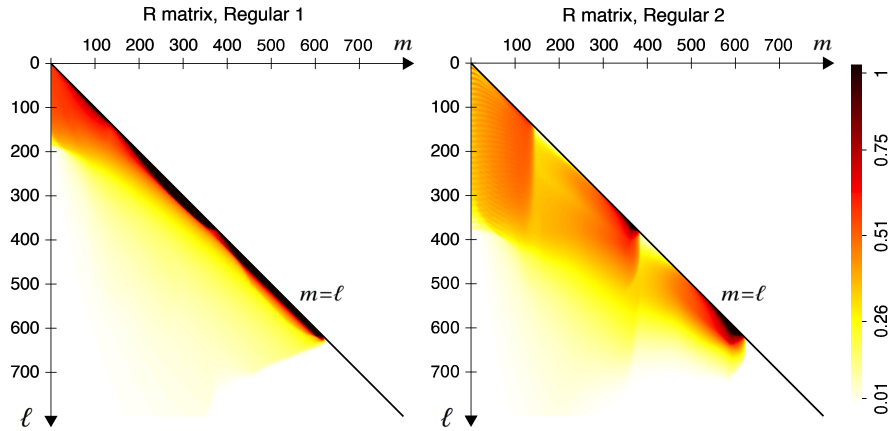

Fig. 5 Comparison of the $\mathcal{R}$ matrix for Regular 1 (*left*) and Regular 2 (*right*) configurations.

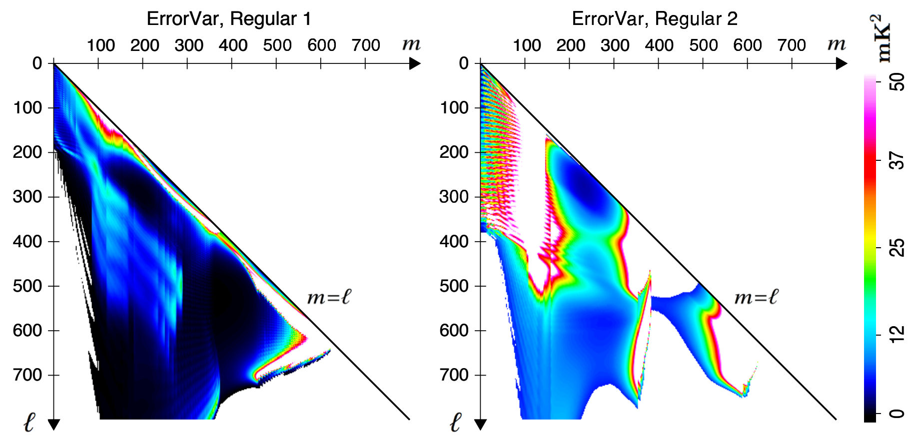

Fig. 6 Comparison of the error variance matrix for Regular 1(*left*) and Regular 2 (*right*) configurations.

not limited to a narrow strip, but is rather a hemisphere or even a larger spherical zone. As such, the cylinder baseline would only be bounded by $m = \ell$.

In the cylinder case, the $\mathbf{R}$ matrix at $m = 0$ is significant up to $\ell \sim 190(380)$ for the Regular 1 (Regular 2) case, which corresponds to the modes probed by the maximum baseline along one cylinder. The longest baselines of the array are however the diagonal ones, i.e. the baselines from the North/South end of the East cylinder to the South/North end of the West cylinder, so the $\mathbf{R}$ matrix is mostly distributed on a band along $m = \ell$, with some extension to higher ℓ in the region between $m = 0$ and $m = \ell$, forming a shark fin shape. The region near $m \sim 0$ is limited to relatively small ℓ due to the fact that our NS baselines are shorter, especially for the Regular 1 case. Future extensions which fill up the remaining part of the cylinder would help improve the $m = 0$ region.

In the Regular 2 case, a larger part of the (ℓ, m) space is covered than in the Regular 1 case, but here the receivers are spread more widely, reducing the density of the baseline coverage, so here there is more apparent non-uniformity, as shown by the vertical stripes at $m = 120$ and 350. These can be understood as follows: as shown in Figure 4, each baseline is sensitive to some part of the (ℓ, m) space. The part of (ℓ, m) space which is not covered by baselines in the array would not be well reconstructed. As the cylinder array is aligned along the three cylinders, we can expect that the m values centered at 0, 235 and 470 will be covered, but regions between these, centered at $m = 120$ and 350, will not be well covered and may have large errors. Furthermore, on careful examination, some fringes near $m = 0$ can also be seen, which may be due to the grating lobes.

Figure 6 shows the corresponding error covariance matrix in the (ℓ, m) basis at 750 MHz. For the Regular 2 case the errors are particularly large, but even for the Regular 1 case, the errors are also relatively large at these m values. The error values at other regions are relatively small. Additionally, in the Regular 2 case, near $m = 0$ there is relatively large error and also the error shows some rapid modulation in ℓ. These fringes are similar to the ones that appear in the $\mathbf{R}$ matrix at the same positions, and are due to the strong grating lobes.

In Figure 7 we show the reconstructed map at 750 MHz derived from simulated observation using the regular cylinder array, ignoring instrument noise. The left

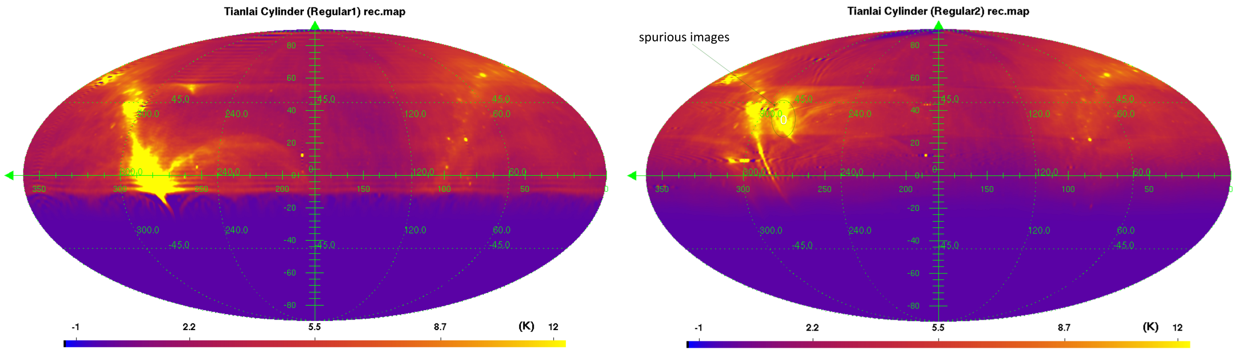

Fig. 7 Reconstructed sky map for the Tianlai cylinder configuration at 750 MHz. *Left*: Regular 1 configuration; *Right*: Regular 2 configuration. The input map is the GSM map at 750 MHz.

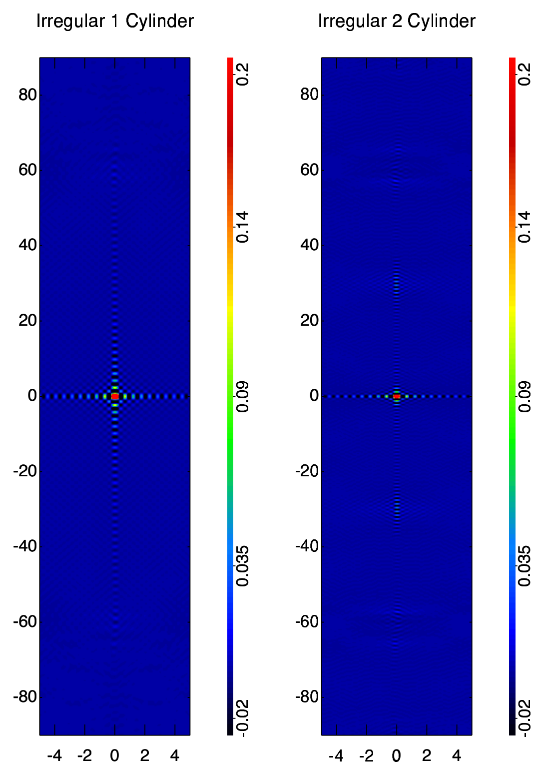

Fig. 8 The synthesized beam for the Tianlai cylinder irregular configuration.

panel uses the Regular 1 configuration, and the right panel uses the Regular 2 configuration.

Comparing with the original map in Figure 2, there are spurious features appearing in the reconstructed map. This is very obvious for the Regular 2 case, and is also present in the Regular 1 case (e.g. the bright spot at $(270°, 54°)$). These are produced by the grating lobes of the brighter sources such as the Galactic plane and strong point sources, and the Regular 2 case is worse than the Regular 1 case. Because of such spurious features, one cannot use an array with such configurations to conduct a reliable sky survey.

4 THE IRREGULAR ARRAY CONFIGURATION

As we saw in the last section, spurious images appeared in the reconstructed maps of the regular array due to the presence of the grating lobes. To avoid this problem, one could adopt spacings less than half a wavelength, or employ non-uniform spacing in the linear array. However, at the wavelength of our observation, it is not practical to have spacing less than half a wavelength. There are many possible non-uniform spacing schemes, and here we choose a very simple one: adopting slightly different spacings on the three different cylinders. So, we take the same total length on the

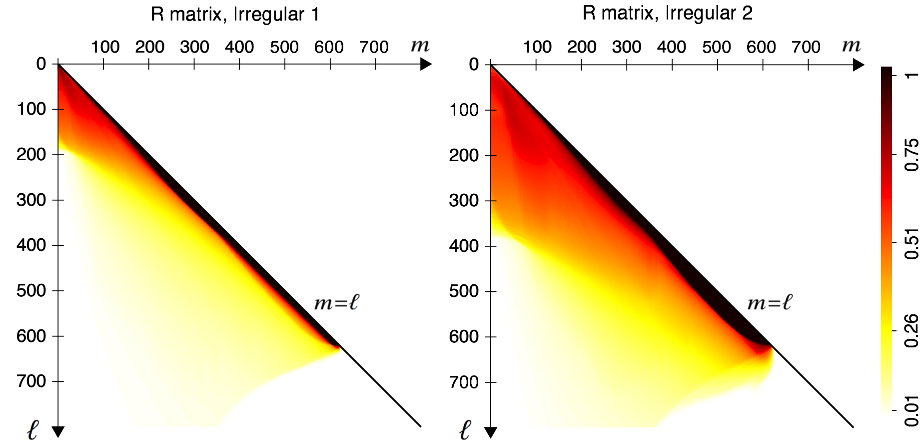

Fig. 9 Comparison of the $\mathcal{R}$ matrix for the Irregular 1 (*left*) and Irregular 2 (*right*) configurations.

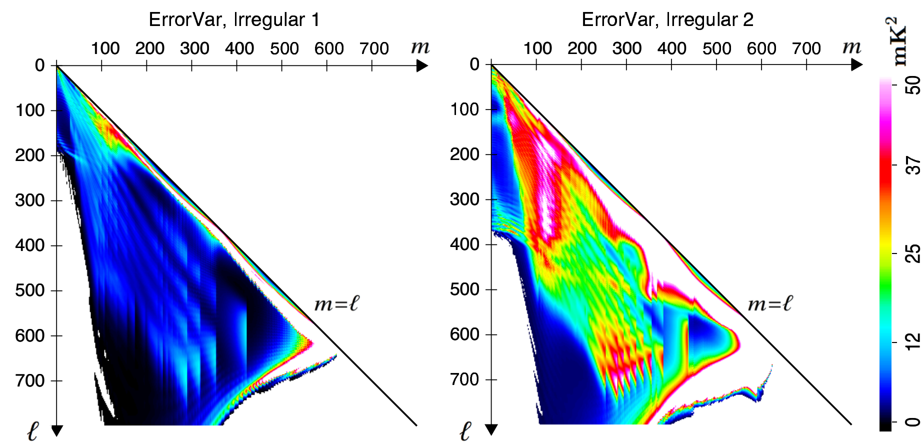

Fig. 10 Comparison of the error variance matrix for irregular configurations.

three cylinders, but place 31, 32 and 33 feeds on each cylinder, so that the unit separations are different in each case. We choose the same two total lengths as the regular cases described in the last section. So for the Irregular 1 case, the basic spacings are $d_{\rm sep} = 0.413, 0.4$ and $0.388\,$m for the three cylinders respectively, with a total length of 12.4 m; for the Irregular 2 case, the basic spacings are 0.827, 0.8 and 0.775 m respectively, with a total length of 24.8 m.

There are still some degeneracies in the NS baseline. For example, there are 30, 31 and 32 instances of $d_{\rm sep} = 0.413, 0.4$ and $0.388\,$m NS baselines in the Irregular 1 configuration, respectively. Nevertheless, for the whole array there are NS baselines with different lengths. The slightly different positioning of the receivers also creates baselines which deviate from the EW direction to different degrees. The whole set up allows wider and more uniform coverage on the (ℓ, m)-plane.

Figure 8 shows the synthesized beam for the two irregular cases. Here we see that the level of grating lobes is greatly reduced. Although in Figure 3 we can clearly see the sharp grating lobes at 28° for the Regular 2 configuration and at 57° for both the Regular 1 and Regular 2 configurations, in Figure 8 at these angles the lobes are barely visible. Of course, there are still the primary beam side lobes, but these are generally much smaller. Here we note that the Irregular 2 lobes are weaker than the Irregular 1 lobes.

In Figure 9, we plot the compressed response matrix $\mathbf{R}(\ell, m)$ for the Irregular 1 (left) and Irregular 2 (right) configurations at 750 MHz. As expected, the general shapes of the (ℓ, m) space distribution are similar for the two cases, but with a wider area covered in the (ℓ, m) space for the Irregular 2 configuration due to the larger array sizes. The broad outline of the shapes in this figure are also similar to those in Figure 5, but here the distribution is more smooth and uniform due to the more widely spread-out (ℓ, m) coverage in the irregular configurations. The features at $m = 120$ and 350 in the Irregular 2 configuration are much less prominent than in the Regular 2 case.

Figure 10 shows the corresponding error covariance matrix in the (ℓ, m) basis. Here the regions with larger error are spread out more widely, but the error value at the maximum is greatly reduced when compared with the reg-

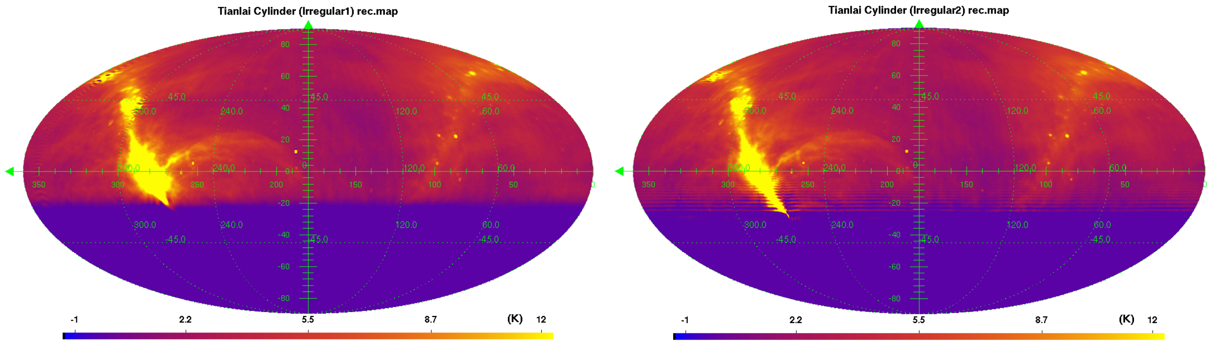

Fig. 11 Reconstructed sky map for the Irregular 1 (*left*) and Irregular 2 (*right*) configurations at 750 MHz.

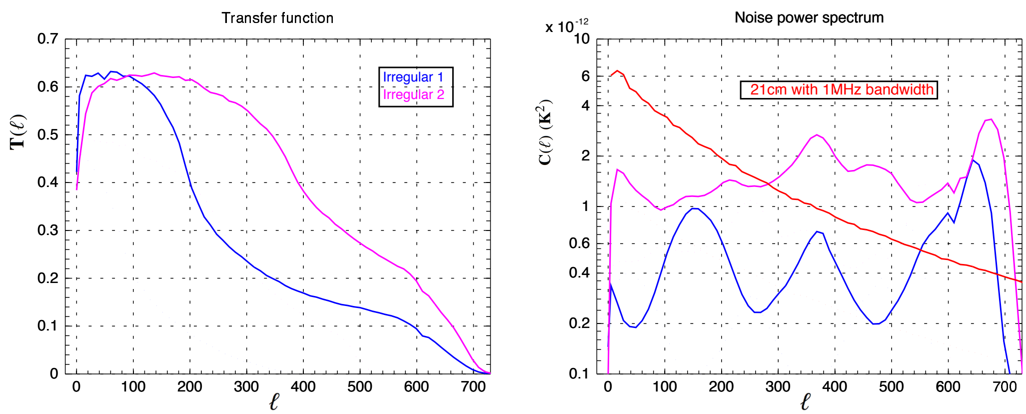

Fig. 12 Comparison of the transfer function $T(\ell)$ (*left panel*) and the noise power spectrum $C^{\rm noise}(\ell)$ (*right panel*) for the Irregular 1 and Irregular 2 configurations.

ular configurations. The Irregular 1 case has smaller errors than the Irregular 2 case because the baselines are more concentrated in the former case which helps reduce the errors.

Figure 11 shows the simulated reconstruction map at 750 MHz with the Irregular 1 (top) and Irregular 2 (bottom) configurations. We can see that in both cases, the reconstruction works relatively well. The spurious features shown in Figure 7 are absent in these figures, and most features in the original map are well reproduced. There are still some regions where the reconstruction shows some artifacts, such as the stripes at $(350°, 60°)$ and $(190°, 12°)$ in the Irregular 1 map, and the stripes South of the equator in the Irregular 2 map. However, the overall quality for the two maps is good.

In Figure 12, we plot the power spectrum transfer function $T(\ell)$ (left panel) and the noise power spectrum (right panel) for the Irregular 1 and Irregular 2 configurations. Here we have masked out the border pixels outside the band $0° < \theta < 105°$ which are not well constructed, and suppressed (ℓ, m) modes with large errors by applying a weight proportional to $\sigma_{\mathcal{I}}^{-2}(\ell, m)$ to all modes which have error larger than $K\sigma_{\rm min}^2$, where $\sigma_{\rm min}$ is the minimum value of the noise covariance matrix, and for the threshold value we choose $K = 50$. The transfer function decreases toward higher ℓ, but it is generally smooth, although there are curvatures at certain values of ℓ. The Irregular 1 configuration has a higher response at lower ℓ, but decreases more rapidly at higher ℓ which is expected, because its baselines are concentrated in smaller regions and are more sensitive to larger angular scales. For the noise power spectrum, we see that the Irregular 1 configuration achieved lower noise power than the Irregular 2 configuration. In both cases the noise power spectrum shows several peaks and troughs, which are due to the different density of baselines on the (ℓ, m) plane. We also draw the expected large scale structure 21 cm signal power on the same plot, where we assume cosmology from Planck Collaboration et al. (2014), and for neutral hydrogen we adopt $\Omega_{\rm HI}b = 0.62\times10^{-3}$ (Switzer et al. 2013). The 21 cm signal is only a few times the noise. Note that because this is for detection at a single frequency, we will have more frequency data, but at the same time there are also complications in foreground removal and calibration, which are beyond the scope of the present work. Considering these factors, we see that detecting the 21 cm signal would be a great challenge.

5 CONCLUSIONS

The Tianlai experiment aims to make a low angular resolution, large sky area transit survey of large scale structures by observing the redshifted 21 cm line from neutral hydrogen. By adopting the transit survey strategy, where the telescope is fixed on the ground and scans the whole observable part of the sky by rotation of the Earth, the cost for building the telescope is reduced, and the instrument is also more stable. The transit scan is however very different from a tracking observation, and for the whole sky survey one must also take into account the sphericity of the sky.

We have developed an efficient, flexible and parallel code to construct a sky map from transit visibilities based on transformations using spherical harmonics. This method is applicable to any transit-type interferometer. This paper is the second in a series of papers presenting our transit array data processing method. In this paper, we have applied this software to simulation of the map-making process for the Tianlai cylinder array pathfinder. In the simulation, we first compute the visibility time streams for several instrument configurations and scanning strategies, and then reconstruct sky maps from these visibilities. The feed response and array geometry are assumed to be known and fully calibrated.

The Tianlai pathfinder has 96 receiver feeds in total, averaging 32 on each cylinder. The cylinders could host about twice that amount of receiver feeds, leaving room for future upgrades after the present hardware design has been thoroughly tested through experimentation. We consider two types of feed arrangements. In one type, the feeds are spaced at about one wavelength, which covers less than half of the cylinder length with the 32 feeds on each. In the other type, 3/5 of the cylinder length is covered, with a spacing of twice the wavelength.

On each cylinder the receiver feeds form regularly spaced linear arrays, which have grating lobes if the unit spacing is larger than half a wavelength. Coupled with the large instantaneous field of view for the cylinder, the grating lobes could be a great obstacle for map-making. To solve this problem, irregular spacing can be introduced. A logistically simple solution is to adopt slightly different unit spacings on the three cylinders, but on each cylinder the spacing is still uniform. We consider the arrangement of 31, 32 and 33 feeds on the three cylinders. With such irregular configurations, the grating lobes are reduced to a very low level and map reconstruction quality is enhanced.

We analyzed the beams produced by the cylinders, and found that features in the response matrix and noise variance matrix can be understood from these. We also computed the transfer function and reconstructed the map for both the Regular and Irregular instrument configurations. We also computed the noise angular power spectrum, which determines the array sensitivity for cosmological 21 cm signal measurement. This may be regarded as a simplification of the real case, where the system temperature is dominated by foreground radiation. We found that for a system temperature of 50 K, the 21 cm angular power spectrum is a few times the noise power in a single 1 MHz narrow band. Detecting such a signal would be a difficult challenge, but the signal may be enhanced by considering joint measurement of the power spectrum over many spectral bins. In the present paper we primarily study the foreground map-making process. Calibration, foreground removal and 21 cm signal extraction will be investigated in subsequent works.

Acknowledgements We would like to thank Ue-Li Pen and Richard Shaw for discussions. The Tianlai project is supported by the MOST 863 program (Grant 2012AA121701) and the CAS Repair and Procurement grant. PAON4 project is supported by PNCG, Observatoire de Paris, Irfu/CEA and LAL/CNRS. JZ was supported by the China Scholarship Council. XC is supported by the CAS Strategic Priority Research Program (XDB09020301), and the National Natural Science Foundation of China (NSFC, Grant 11373030). FW is supported by the NSFC (Grant 11473044).

References

Ansari, R., Le Goff, J. ., Magneville, C., et al. 2008, arXiv:0807.3614

Ansari, R., Campagne, J. E., Colom, P., et al. 2012, A&A, 540, A129

Bandura, K., Addison, G. E., Amiri, M., et al. 2014, in Proc. SPIE, 9145, Ground-based and Airborne Telescopes V, 914522

Barata, J. C. A., & Hussein, M. S. 2012, Brazilian Journal of Physics, 42, 146

Battye, R. A., Browne, I. W. A., Dickinson, C., et al. 2013, MNRAS, 434, 1239

Chang, T.-C., Pen, U.-L., Peterson, J. B., & McDonald, P. 2008, Physical Review Letters, 100, 091303

Chen, X. 2012, International Journal of Modern Physics Conference Series, 12, 256

Chen, X. 2015, IAU General Assembly, 22, 2252187

Connor, L., Lin, H.-H., Masui, K., et al. 2016, MNRAS, 460, 1054

de Oliveira-Costa, A., Tegmark, M., Gaensler, B. M., et al. 2008, MNRAS, 388, 247

Feng, L., Vaulin, R., & Hewitt, J. N. 2014, arXiv:1405.6219

Gong, Y., Chen, X., Silva, M., Cooray, A., & Santos, M. G. 2011, ApJ, 740, L20

Górski, K. M., Hivon, E., Banday, A. J., et al. 2005, ApJ, 622, 759

Masui, K., Lin, H.-H., Sievers, J., et al. 2015, Nature, 528, 523

Peterson, J. B., Bandura, K., & Pen, U. L. 2006, astro-ph/0606104

Planck Collaboration, Ade, P. A. R., Aghanim, N., et al. 2014, A&A, 571, A16

Seo, H.-J., Dodelson, S., Marriner, J., et al. 2010, ApJ, 721, 164

Shaw, J. R., Sigurdson, K., Pen, U.-L., Stebbins, A., & Sitwell, M. 2014, ApJ, 781, 57

Switzer, E. R., Masui, K. W., Bandura, K., et al. 2013, MNRAS, 434, L46

Xu, Y., Wang, X., & Chen, X. 2015, ApJ, 798, 40

Yu, H.-R., Zhang, T.-J., & Pen, U.-L. 2014, Physical Review Letters, 113, 041303

Zhang, J., Ansari, R., Chen, X., et al. 2016, arXiv:1606.03090